JGR Oceans

RESEARCH ARTICLE
10.1029/2023JC019948

Key Points:
- SWIFT buoy data show that frequency dependence of wave attenuation in Antarctic sea ice follows a power law
- Both wave attenuation and the frequency dependence of attenuation were stronger in austral winter than in spring
- Observations suggest a change in wave direction in sea ice compared to open water

Supporting Information:

Supporting Information may be found in the online version of this article.

Correspondence to:

S. Wahlgren,
stina.wahlgren@gu.se

Citation:

Wahlgren, S., Thomson, J., Biddle, L. C., & Swart, S. (2023). Direct observations of wave-sea ice interactions in the Antarctic marginal ice zone. *Journal of Geophysical Research: Oceans*, *128*, e2023JC019948. https://doi.org/10.1029/2023JC019948

Received 19 APR 2023
Accepted 20 SEP 2023

Direct Observations of Wave-Sea Ice Interactions in the Antarctic Marginal Ice Zone

S. Wahlgren[1], J. Thomson[2], L. C. Biddle[1], and S. Swart[1,3]

[1]Department of Marine Sciences, University of Gothenburg, Gothenburg, Sweden, [2]Applied Physics Laboratory, University of Washington, Seattle, WA, USA, [3]Department of Oceanography, University of Cape Town, Rondebosch, South Africa

Abstract

Wave energy propagating into the Antarctic marginal ice zone effects the quality and extent of the sea ice, and wave propagation is therefore an important factor for understanding and predicting changes in sea ice cover. Wave-sea ice interactions are notoriously hard to model and in situ observations of wave activity in the Antarctic marginal ice zone are scarce, due to the extreme conditions of the region. Here, we provide new in situ data from two drifting Surface Wave Instrument Float with Tracking (SWIFT) buoys deployed in the Weddell Sea in the austral winter and spring of 2019. The buoy location ranges from open water to more than 200 km into the sea ice. We estimate the attenuation of swell with wave periods 8–18 s, and find an attenuation coefficient $\alpha = 4 \cdot 10^{-6}$ to $7 \cdot 10^{-5}$ m^{-1} in spring, and approximately five-fold larger in winter. The attenuation coefficients show a power law frequency dependence, with power coefficient close to literature. The in situ data also shows a change in wave direction, where wave direction tends to be more perpendicular to the ice edge in sea ice compared to open water. A possible explanation for this might be a change in the dispersion relation caused by sea ice. These observations can help shed further light on the influence of sea ice on waves propagating into marginal ice zones, aiding development of coupled wave-sea ice models.

Plain Language Summary

Changes in the sea ice extent around Antarctica affects the global climate, and it is therefore important to accurately represent sea ice in climate models. One feature that is generally missing in climate models is the interaction between ocean waves and sea ice. Ocean waves change the sea ice, for example, by breaking up ice floes into smaller ones. At the same time, the sea ice reduces the strength of the waves so that the wave height decreases and eventually disappears far into the sea ice. How far into the sea ice waves reach depends both on the size of the waves and on the sea ice, and can be very different depending on for example, ice thickness, size of floes and age. In order to better represent the wave-sea ice interactions in climate models, simple but accurate models of how fast sea ice reduces the strength of waves is needed. Using wave buoys, we measured the wave activity in the Antarctic sea ice during two expeditions in 2019. We found a notable difference between spring and winter, where the waves were reduced much faster in winter than in spring. This can help to improve predictions of sea ice cover.

1. Introduction

The sea ice around Antarctica is important for global climate in several ways. Loss of Antarctic sea ice has been linked to ice shelf disintegration, by allowing storm-induced swell waves to reach exposed ice shelf fronts, leading to accelerating loss of the Antarctic ice sheet and increase in sea level rise (Massom et al., 2018). The growth and melt of sea ice acts as a freshwater sink/source, and ocean-atmosphere interactions, such as exchange of heat or momentum, are also affected by the ice condition (Vichi et al., 2019). The transition between the open ocean and pack ice is called the marginal ice zone (MIZ). Multiple definitions of the MIZ exist, depending on purpose and field of study it can be defined based on wave activity as a region where waves and sea ice co-exist (Squire, 2022), based on sea ice concentration (Vichi, 2022) or based on other properties of the ice, such as thickness or floe size distribution. In the Antarctic the width of this zone can be hundreds of kilometers (Brouwer et al., 2022).

One factor that influences the MIZ and its sea ice condition is surface gravity waves. Waves affect ice formation (Shen & Ackley, 1991) and can break big ice floes into smaller ones (Langhorne et al., 1998), altering dynamical properties and heat exchange. One key property determining to what extent this happens is the significant wave height (Toffoli et al., 2015). In return, the MIZ also affects surface waves by attenuating them, thus influencing how far into the ice the waves reach and can affect the sea ice. Incorporating coupled sea ice-wave models into climate models is therefore important for improving predictions of for example, MIZ extent and distribution. Yet, wave-ice coupling is still generally neglected in polar climate modeling (Kousal et al., 2022). Lack of observations also leaves weak constraints on coupled sea-ice models (Cooper et al., 2022), meaning that future predictions and current parameterizations have large uncertainties. Poor constraints in sea ice concentration are also associated with large uncertainties in wave modeling (Nose et al., 2020).

It is well established that the amplitude of waves decreases with distance traveled in ice, and that the sea ice acts as a low-pass filter, attenuating higher frequency waves more rapidly than waves with lower frequencies. The exact nature of the attenuation, and how much of it that can be attributed to energy dissipation versus scattering, has long been debated, but recent observations point to dissipation as the dominant factor in the MIZ, where the wave length is generally much larger than the floe size (Ardhuin et al., 2020; Squire, 2022; Voermans et al., 2019). Waves traveling into the MIZ are typically thought to decay exponentially, which was first reported in Wadhams et al. (1988) based on several field experiments in the Arctic MIZ. Since then, many studies have reproduced this result.

The frequency dependence of the attenuation is typically modeled as a power law dependence, or as a sum of power laws. Different physical processes are expected to result in different frequency dependence. Observations from both the Arctic and the Antarctic MIZ consistently shows a power coefficient between 2 and 4 (Meylan et al., 2018), affected by physical parameters such as sea ice type and concentration, floe size and wave period (Kohout et al., 2020; Meylan et al., 2018; Montiel et al., 2022). Thicker sea ice appear to attenuate waves faster (Rogers et al., 2021), and for vertically layered sea ice, for example, pancake ice on top of grease ice, attenuation scales with the total thickness rather than that of a single layer (De Carolis et al., 2021). Further, Ardhuin et al. (2020) emphasize that attenuation mechanisms differ vastly between the outer break-up region, where waves cause the sea ice to form floes, and the inner region with continuous ice sheets. Wind direction can also influence attenuation, where head-wind has been observed to increase attenuation (Montiel et al., 2022) and strong winds have been shown to be able to transfer energy to waves even on fully ice covered areas (Alberello et al., 2022).

Observations of frequency dependence attenuation in the Antarctic MIZ are scarce. Meylan et al. (2014) described the attenuation coefficient for wave periods 2–20 s as a sum of two power laws of order 2 and 4, based on data from an array of 5 wave buoys deployed in September 2012 during the SIPEX-II campaign. The most extensive wave buoy data set is from the PIPERS expedition, where 14 buoys were deployed in the Ross Sea, collecting data between April and July 2017 (Kohout et al., 2020). Neither of these wave buoys provide wave direction. Rogers et al. (2021) used a subset of the PIPERS data set, collected in June 2017. Montiel et al. (2022) found a power coefficient 2.5 based on another subset of the PIPERS data set collected in April–May 2017.

In this study we present new wave buoy data from the Weddell Sea. We use this to derive frequency dependent attenuation of swell waves in the Antarctic MIZ for both austral winter and spring. We also show a difference in wave direction in sea ice and open water that might be attributed to a change in the dispersion relation.

2. Materials and Methods

2.1. SWIFT Buoy and Deployments

We use data from two SWIFT v3 buoys (Thomson, 2012) deployed in the MIZ in the Southern Ocean as part of the ROAM-MIZ project (www.roammiz.com) (Swart et al., 2020) during the SCALE research voyages in 2019 (Ryan-Keogh & Vichi, 2022). The buoys were equipped with GPS logger, inertial measurement units (IMU), meteorological stations (airmar WX-200 Ultrasonic weather stations) and a low resolution camera. The two buoys, here referred to as SWIFT20 and SWIFT21, were deployed in austral winter (27–28 July) and austral spring (23 October–7 November). They recorded a total of 17 days of data (16 days simultaneously with both buoys) with different ice types and weather conditions. SWIFT buoys are deployed directly into the water, and measure wave periods in the range 2–20 s, corresponding to wavelengths 6–600 m in deep open water. This covers all but the highest frequencies of the wind-wave interactions.

Initial local conditions varied between the two seasons, both in sea ice type and atmospheric variability. During the winter deployment, the sea ice field was largely composed of unconsolidated pancake ice floes, generally of 1–5 m diameter and around 40 cm thickness (Skatulla et al., 2022). Open water regions between the floes was often occupied by grease or frazil ice. These cold, ice forming conditions were reflected in the air temperature recorded by the SWIFT buoys during deployment (Figure 4g), with temperatures well below −10°C. SWIFT20

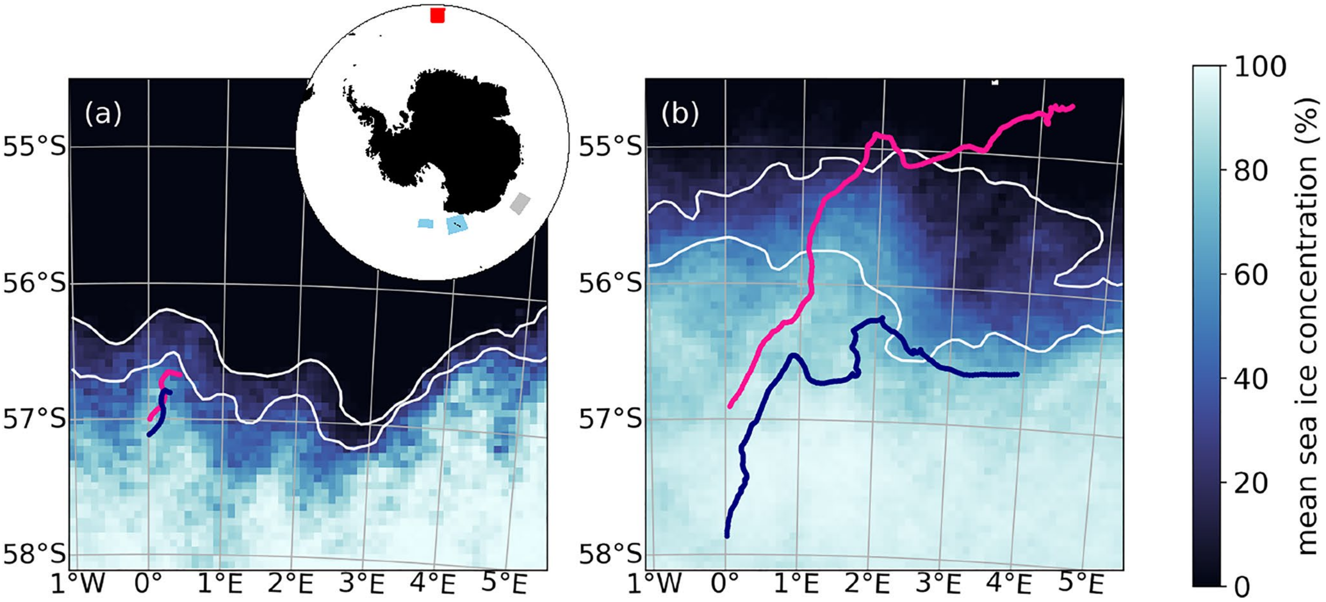

Figure 1. Overview of the two SWIFT deployments. Average sea ice concentration over the time span the buoys were deployed, together with tracks for SWIFT20 (pink) and SWIFT21 (blue), during (a) winter deployment and (b) spring deployment. Sea ice edges of the minimum (27 July, 23 October) and maximum (28 July, 4 November) sea ice extents during the deployments are shown in white. Inset: Geographic location of the SWIFT deployments (red), together with the locations of the PIPERS data set (light blue) (Kohout et al., 2020) and SIPEX II data set (gray) (Meylan et al., 2014).

was deployed at 57°S, 0°E, approximately 25 km into the sea ice pack. SWIFT21 was deployed approximately 10 km south of SWIFT20, further into the sea ice field, and they stayed approximately 10 km apart while drifting north (Figure 1a). Photos of the ice taken from the ship are provided by de Vos et al. (2019). The edge of the MIZ was further south in the winter than during the spring deployment, and was advancing north during and after the winter deployment.

In spring, a strong diurnal cycle was present in the air temperatures, with temperatures reaching or surpassing 0°C frequently (Figure 4g). The sea ice was covered with a snow layer (Johnson et al., 2023), and consisted of larger, consolidated ice floes. SWIFT20 was deployed at the same site as the winter deployment, which was then around 100 km from the ice edge. SWIFT21 was deployed around 100 km south of SWIFT20 (Figure 1b), in the ship track in densely packed, consolidated ice floes. Again, both buoys drifted north. After approximately 9 days, SWIFT20 drifted out of the ice into open water, while SWIFT21 stayed in the sea ice during the deployment. On recovery of SWIFT21, the sea ice consisted of ice floes with clear open water between. Photos from deployment and recovery are presented in Supporting Information S1 (Figures S1–S3).

2.2. Wave Spectrum

SWIFT buoys estimate the wave field by measuring the horizontal (GPS) velocity and vertical (IMU) acceleration of the buoy. Raw motion data are recorded at 4 Hz for bursts lasting 512 s and an interval of 720 s. The power spectral density, $E(f)$, is estimated using 256 s windows with 75% overlap and a variance-preserving taper. Every three neighboring frequency bands are merged, such that the resulting spectral estimates have 12 degrees of freedom. The use of GPS velocities assumes circular orbital motion (Thomson et al., 2018), which is predicted by linear wave theory for waves in deep open water. The validity of this assumption is measured with the check factor, which is simply the ratio between the measured horizontal and vertical displacement (Thomson et al., 2015). This ratio should be equal to 1, and large deviations from this indicates that the measurement is not reliable.

Significant wave height, H_s, is computed from the wave spectrum with

$$H_s = 4 \cdot \sqrt{\int_{f_1}^{f_2} E(f)\,df} \tag{1}$$

Data with $H_s < 0.1$ m is not used in further analysis due to low signal-to-noise ratio (SNR).

In addition to the 1D wave spectrum, SWIFT buoys provide the standard directional moments of the spectrum (a_1, b_1, a_2, b_2). The dominant direction for each frequency bin can be estimated using the first directional moments a_1 and b_1 (see the appendix in Thomson et al. (2018) for details). We define the mean wave direction, Θ, for a frequency band limited by f_1, f_2 as the energy weighted dominant direction

$$\Theta = \arctan\left(\bar{b}_1, \bar{a}_1\right) \tag{2}$$

where

$$\bar{a}_1 = \frac{\int_{f_1}^{f_2} E(f) a_1(f)\,\mathrm{d}f}{\int_{f_1}^{f_2} E(f)\,\mathrm{d}f} \tag{3}$$

is the energy weighted directional moment. The direction is then converted to nautical convention (clockwise, 0 at north) and defined as the direction the waves are heading toward. The spread of the mean direction, ΔΘ, is computed as

$$\Delta\Theta = \sqrt{2\left(1 - \sqrt{\bar{a}_1^2 + \bar{b}_1^2}\right)}. \tag{4}$$

2.3. Defining the Ice Edge

In order to determine the distance traveled by waves in sea ice, we need to estimate the location of the transition between open water and the MIZ, here called the sea ice edge. We estimate the ice edge based on AMSR2 sea ice concentration (SIC). The data set had a spatial resolution of 6.25 × 6.25 km and provided daily (Melsheimer & Spreen, 2019).

The ice edge was detected from sea ice concentration as follows: for each time instance, a binary map was created, with zeros where sea ice concentration was less than 15% and ones where sea ice concentration was 15% or more. The binary map was then smoothed using a 2D Gaussian filter with a standard deviation σ_{edge} of 1 pixel (6.25 km), and the ice edge was defined as the 0.5 contour line of the smoothed map. An example of sea ice concentration and derived ice edge is shown in Figure 2a.

The derived ice edge was compared to SAR images (GRD, HH-band) from Sentinel-1 (0.1 × 0.1 km, 6 days resolution) when available in our study region. The ice edge and SAR images showed good agreement on a large scale, but there are areas outside the ice edge where streaks of ice (0.1–1 km wide) are visible in the SAR imagery (Figure 2b). A limitation with AMSR2 is that it does not capture small scale variations in ice coverage well, and those streaks are not visible in the AMSR2 data (2a). However, due to their limited size, the influence of those ice streaks on swell waves is small (causing an error in the attenuation coefficient estimation of 1% for measurements 100 km into the sea ice.)

The ice edge was roughly aligned in the east-west direction, but was observed to be very dynamic in its orientation and location. The ice edge shifted more than 100 km north during the first 6 days of the spring deployment (Figure 2c), and around 40 km north during the 2 days long winter deployment (Figure 1a), illustrating that the Antarctic MIZ is prone to large spatial changes over short periods. Those rapid shifts are likely caused by ice drift rather than freezing, as the buoys drifted north in a similar manner to the ice edge shift. The effect of surface winds and their ability to cause rapid changes to the Antarctic MIZ has recently been discussed in Womack et al. (2022).

2.4. Local Ice Condition

In addition to co-located AMSR2 sea ice concentration data, imagery from cameras mounted on the masts of the SWIFT buoys were used to categorize the local ice condition (Figure 3). The cameras were approximately 1 m above the surface, and captured one photo every 4 s for the first 8 min of every hour. The images were analyzed manually. Photos captured during the dark hours (around 8p.m.–4a.m. UTC for the spring deployment, and

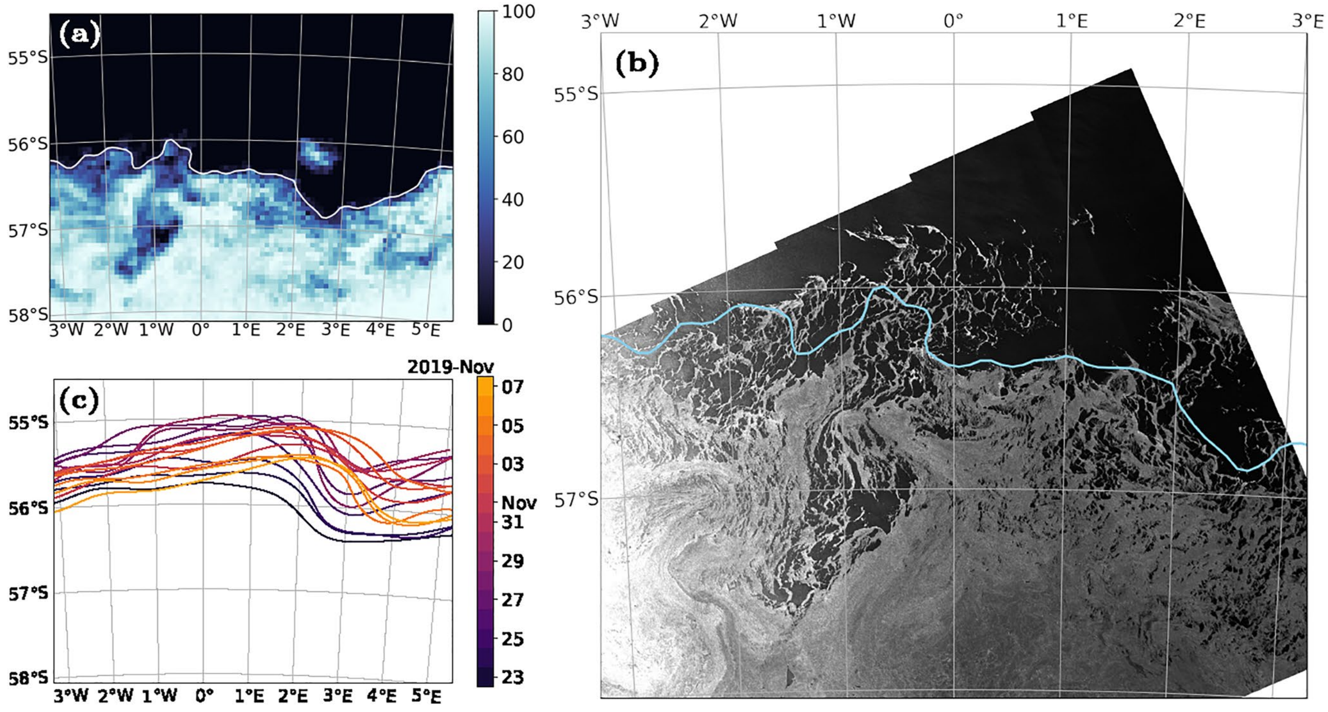

Figure 2. Locating the ice edge from AMSR2 sea ice concentration. (a) Example of ice edge (white) derived from AMSR2 sea ice concentration. (b) Comparison between the derived ice edge and Sentinel-1 SAR imagery (HH band). (c) The movement of the ice edge during the spring deployment. For illustration purposes, a smoother version of the edge ($\sigma_{\text{edge}} = 37.5$ km) is shown.

around 6p.m.–7a.m. for the winter deployment), as well as blurry photos were discarded. The blurriness often occurred during morning hours and typically disappeared after a couple of hours, probably due to ice on the lens. Time lapses of the imagery are provided in Movies S1–S3.

Due to limitations of the imagery, the standard ice scale Antarctic Sea Ice Processes and Climate (ASPeCT) protocol (Worby & Allison, 1999) was not applicable. The main limitations are a limited field of view and no available size reference (except for a few feathery friends—Figure 3), which makes it hard to determine ice thickness and floe size. An ice type scale designed specifically for SWIFT imagery was introduced in Rogers et al. (2018) (Hošeková et al., 2020), but this only covers pancake ice. Instead, we did a coarse classification of ice condition into four groups: continuous ice/very large ice floes, ice floes approximately 1–10 m, brash and open water (Figure 4).

2.5. Distance to the Edge

The peak wave direction measured with SWIFT was generally toward south east, indicating an oblique incidence from the ice edge. We use two different measures of distance to the ice edge: the meridional distance to the edge and the distance in respect to the wave direction. The latter one is the one that matters for wave attenuation, but it is also sensitive to errors in estimated wave direction. For determining wave direction, the energy-weighted mean wave direction was used, as defined in Equation 2 at the buoy location. Distance in wave direction was not computed for data points with $H_s < 0.1$ m, since no reliable wave direction could be derived for those points.

Distance was determined in AMSR2 sea ice concentration coordinates. This is a polar stereographic projection, referenced at 70°S, 0°E (Melsheimer, 2019), thus giving a distortion of 11%–12% at the buoy location. Compared to other uncertainties, this is small and therefore not accounted for.

2.6. Wave Attenuation

We derive spectral wave attenuation assuming exponential decay with distance:

$$E(d, f) = E_0(f)e^{-\alpha(f)d} \tag{5}$$

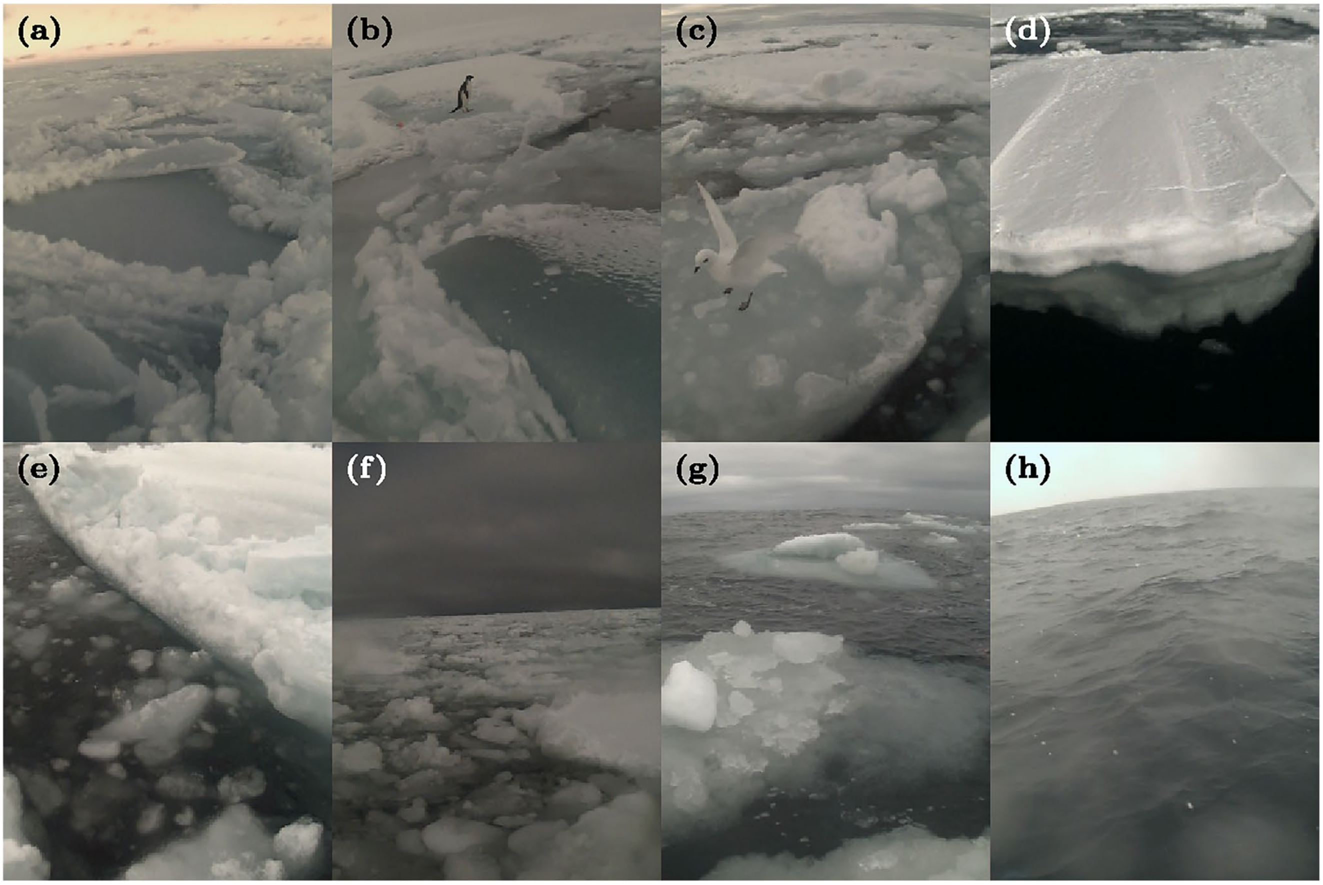

Figure 3. Examples of SWIFT on-board imagery. (a) During the winter deployment, the ice field consisted of pancake and grease ice. During the spring deployment the buoys encountered a wide range of ice conditions: (b) continuous ice, (c–e) ice floes, (f–g) brash and (h) open water. Time lapses of all on-board imagery are provided in Movies S1–S3.

where $\alpha(f)$ is the (frequency dependent) attenuation coefficient, $E_0(f)$ the power spectral density at a reference point and $E(f)$ is the power spectral density after attenuation by sea ice during a distance d. There is an implicit assumption that the attenuation coefficient does not change over the distance d.

We only use data where we have data from both buoys and where both buoys recorded a significant wave height of at least 0.1 m. During the spring deployment, SWIFT21 was deep in sea ice and did not record almost any wave activity for the first part of the deployment (Figure 4). We therefore only use data from 31 October 2019 to 8 November 2019, where SWIFT21 generally observed wave activity and SWIFT20 was in open water. The check factor was generally $\ll 1$ when $E(f) < 10^{-4}$ m^2/Hz, which was true for most part of the spectrum in sea ice (Figure 4). We attribute this to wave attenuation below the instrument noise level, and therefore only focus on the frequency band $0.05 \leq f \leq 0.13$ Hz for this study. In total, this filtering resulted in 36 data point pairs in winter and 100 data point pairs in spring, for each of the seven analyzed frequency bins.

For each pair of data points, the attenuation coefficient was defined as

$$\alpha(f) = \frac{\ln(E_{\text{SWIFT20}}(f)) - \ln(E_{\text{SWIFT21}}(f))}{d} \tag{6}$$

where the power spectral density measurement by SWIFT20 was used as the reference value. In winter, both buoys were in the ice, and we defined d as the effective separation between the both buoys along the incident wave direction. For each time stamp, we defined the incident wave direction as the average of the energy weighted wave direction between the two buoys. In spring, SWIFT20 was in open water, and d was then defined as the distance from SWIFT21 to the ice edge in the energy weighted wave direction as measured in sea ice by SWIFT21.

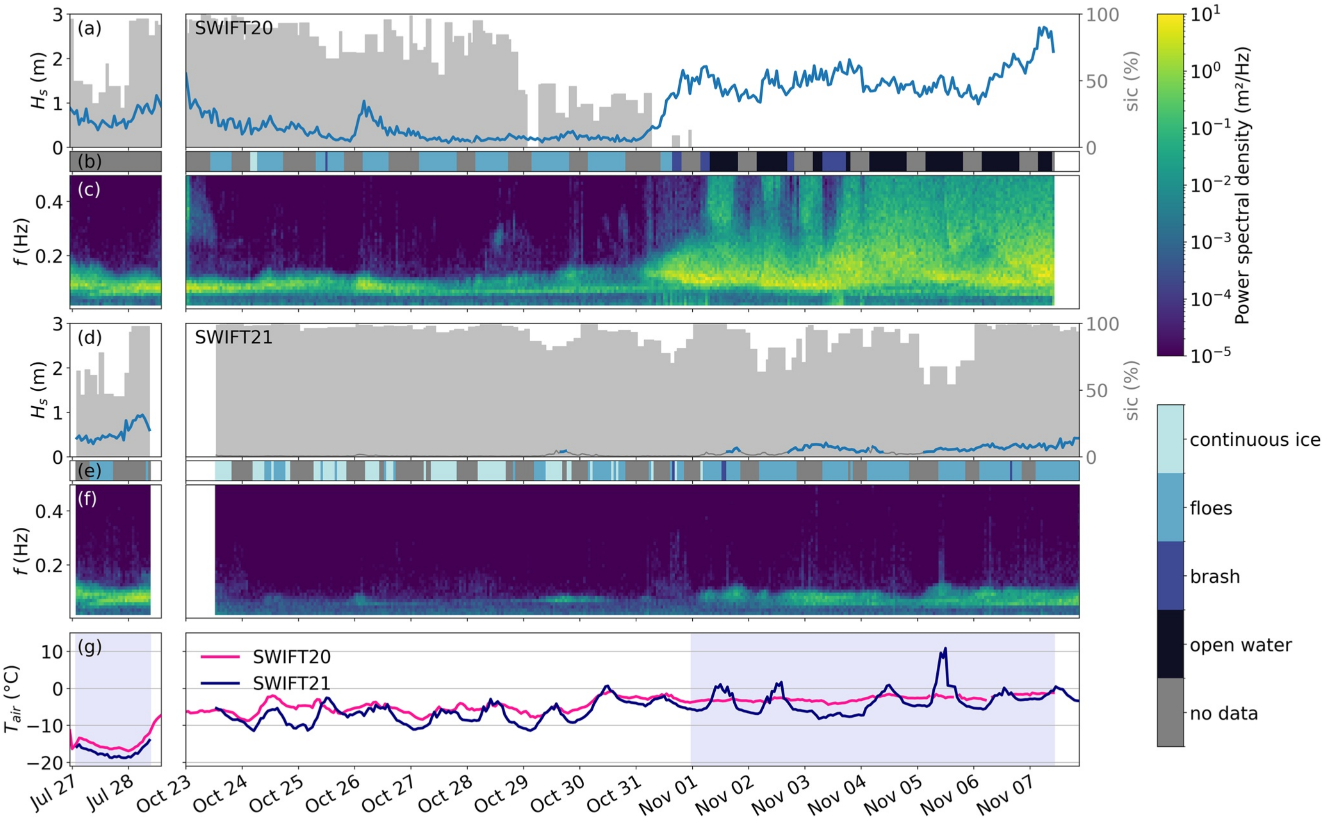

Figure 4. Overview of the data collected by SWIFT20 (top) and SWIFT21 (bottom) in winter (left panels) and spring (right panels). (a, d) Significant wave height (blue line) and wave spectra measured by SWIFT, together with co-located sea ice concentration (shaded gray) from AMSR2. Significant wave height of less than 0.1 m is shown in gray. (b, e) Local ice condition based on SWIFT on-board imagery. (c, f) Spectral power density. (g) Air temperature, measured by the buoys. Shaded areas show the part of the data set that is used for deriving spectral attenuation.

We did not account for the time it would take for waves to travel the effective separation between SWIFT20 and SWIFT21. For the analyzed frequency band, this corresponds to a time delay of 2–5 hr per 100 km based on the dispersion relation for linear waves in deep water. In winter, the buoys were so close that this time lag is shorter than the time resolution. Even though the time lag in spring is large, the temporal variation in spectral energy density is small compared to the difference between buoys. The effect of the time delay on the estimated attenuation coefficient is therefore expected to be small compared to other uncertainties.

3. Result and Discussion

The significant wave height measured by the buoys were around 0.5–1 m during the winter deployment. In spring, SWIFT20 generally measured significant wave heights around 0.2 m while in ice, with two wave events where the significant wave height increased to almost 1 m (Figure 4). While in open water, SWIFT20 measured significant wave heights between 1.5 and 3 m, which is lower than the mean of the region in austral summer (Young et al., 2020). SWIFT21 was arguably not in the MIZ during the first 9 days as almost no wave activity was recorded (Figure 4).

The maximum observed wave height was 2.7 m in open water (SWIFT20, 17 November) and 1.7 m in ice (SWIFT20, 23 October). No significant wave activity was observed more than 200 km from the ice edge in wave direction (150 km from ice edge in southwards direction) (Figures 5a and 5b). Wave activity was observed in 100% sea ice concentration (Figure 4), illustrating that waves can reach beyond the sea ice concentration-based definition of the MIZ.

The measured wave spectra and significant wave height show some of the key effects sea ice has on surface waves. In the ice, the significant wave height is typically much lower (Figures 5a and 5b), and the high frequency

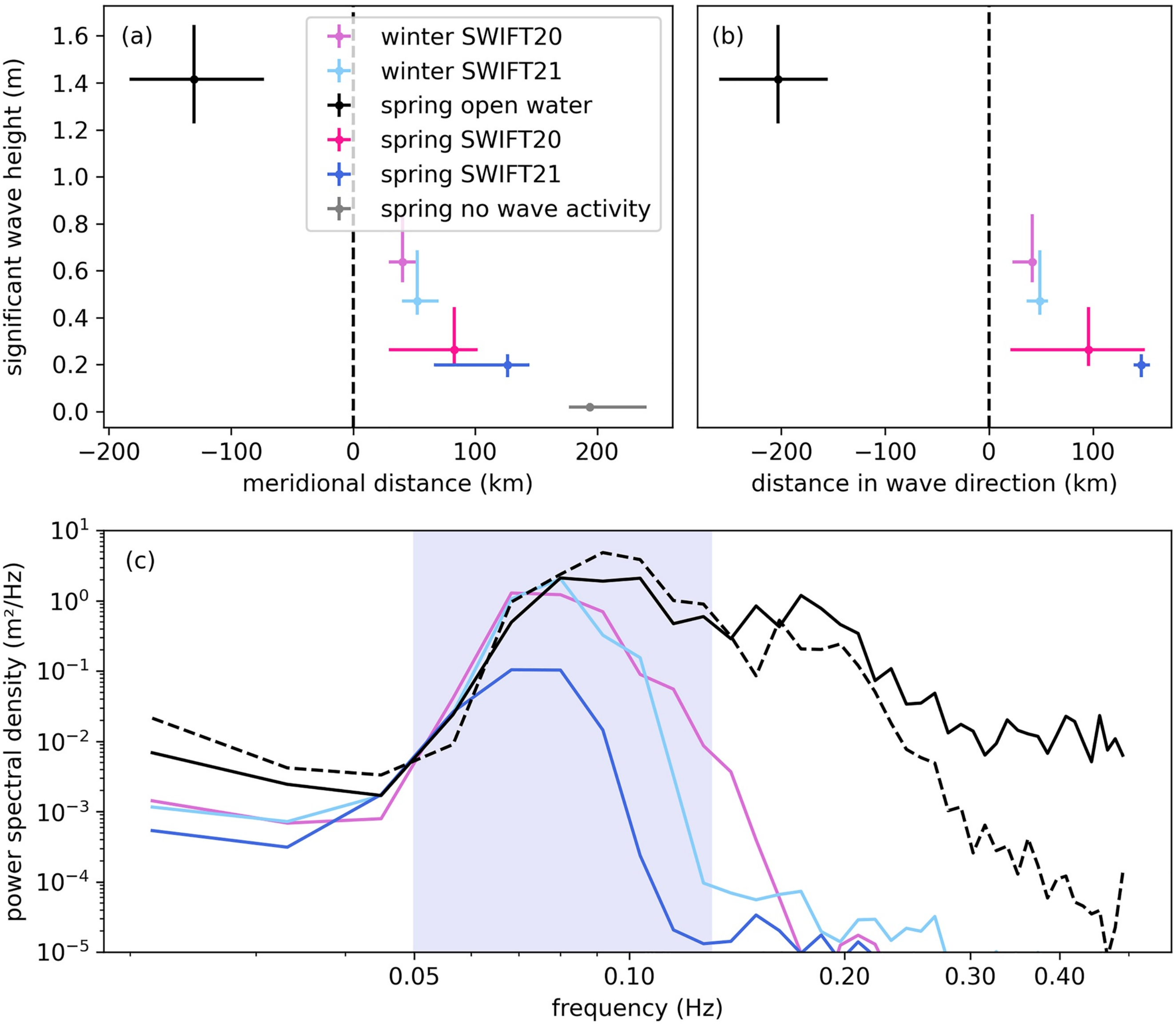

Figure 5. (a) Median and quartiles of significant wave height for all four deployments as a function of meridional distance to ice edge. The SWIFT20 spring deployment is split into in-ice (SIC ≥ 15%) and open water (SIC < 15%). Data with no measurable wave activity ($H_s < 0.1$ m) is shown in a separate category. (b) Same as (a), but as a function of distance to the ice edge in the energy-weighted wave direction. (c) Examples of power density spectra collected in ice in winter by SWIFT20 (pink) and SWIFT21 (light blue), in ice in spring by SWIFT21 (blue), in spring in open water (black) and in open water ice streak (dashed black). The shaded area marks the frequency range used when deriving wave attenuation.

content diminishes (Figures 4c and 4f). The high frequency tail of the measured spectra can be contaminated by noise (Thomson et al., 2021), and thus analysis herein is limited to the shaded region of the spectra in Figure 5c. Above these frequencies, noise can alter the frequency dependence of attenuation and cause an apparent rollover in attenuation (Thomson et al., 2021).

One notable event is the transition from sea ice to open water by SWIFT20 around 31 October. This event is seen as a steep increase in significant wave height as well as an increase in higher frequency content of several orders of magnitude, and is confirmed by SWIFT on-board imagery (Figures 4a–4c). It coincides fairly well with the co-located sea ice concentration. Between 2 and 4 November, when SWIFT20 is in open water, there are three instances where the high frequency content drops. The first one occurred during the dark hours, thus lacking on-board imagery, but for the other two on-board imagery confirms that this is due to sea ice. Those sea ice patches are not seen in the sea ice concentration, and are likely ice streaks similar to the ones visible in Figure 2b. The lower part of the wave spectrum is not affected (Figure 5c).

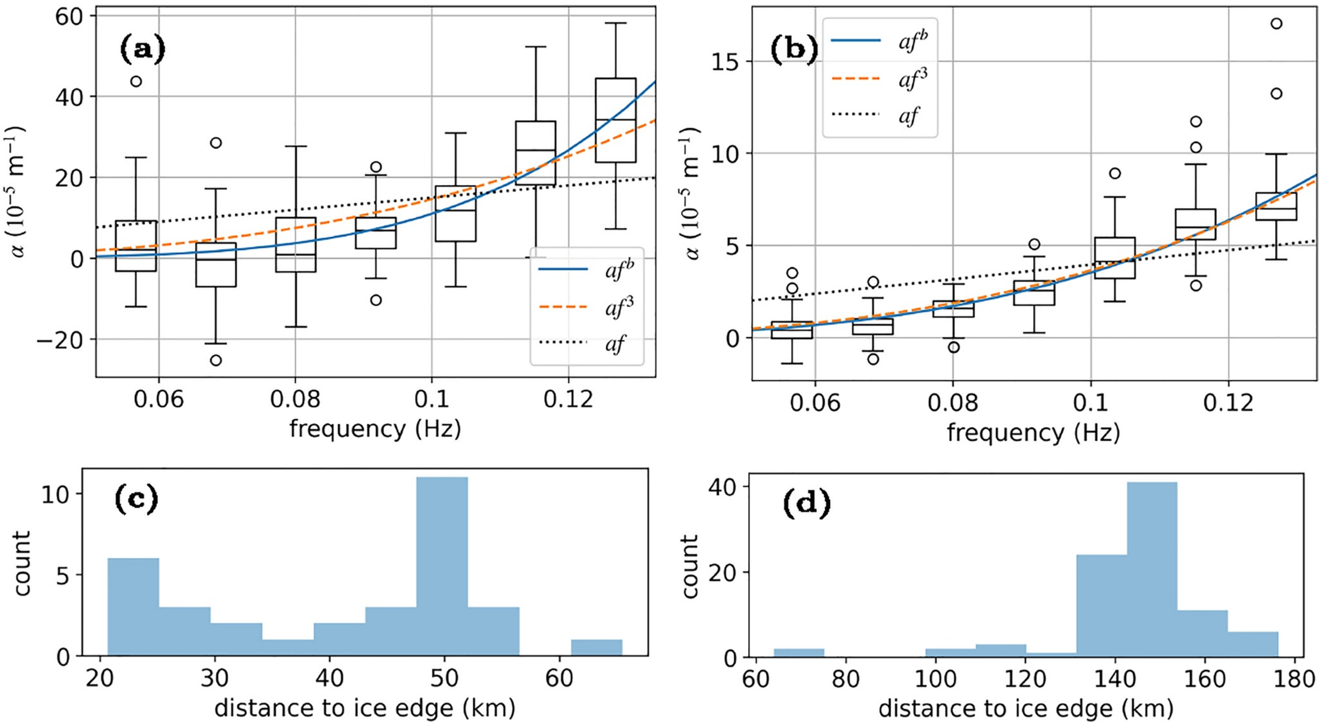

Figure 6. (top) Box-and-whisker plots of the attenuation rates as a function of wave frequency, together with power law-fits. The fitted parameters are presented in Table 1. (a) Data from the winter deployment, where the distance in wave direction between the buoys was around 16 km. Each frequency bin has 36 data points. (b) Data from the spring deployment, where one buoy was in open water and the other in sea ice. Each frequency bin has 100 data points. (bottom) Histogram of the distance in wave direction to the ice edge for the two data sets in (c) winter (mean of the two buoys) and (d) spring.

3.1. Spectral Wave Attenuation

Box-and-whisker plots of the observed attenuation coefficients is shown in Figure 6, together with non-linear least square fits to the power law

$$\alpha(f) = af^{b} \tag{7}$$

The fitted parameters are presented in Table 1. A clear trend with increasing attenuation for increasing frequencies is seen.

Attenuation rates for both spring and winter are in the order of magnitudes $10^{-6} - 10^{-4}$ m^{-1}, consistent with previous observations in the Pacific Antarctic MIZ (Figure 7).

Table 1
Parameter Estimates for the Power Law $\alpha = af^{b}$, Using Non-Linear Least Squares With Various Constraints

Deployment	Constraint	a	b	RMSE (10^{-5} m^{-1})
Spring	None	0.063	3.3	1.22
Spring	$b = 3$	0.036	–	1.23
Spring	$b = 1$	0.0004	–	2.02
Winter	None	8.4	4.9	10.9
Winter	$2 \le b \le 4$	1.3	4.0	11.0
Winter	$b = 3$	0.15	–	11.4
Winter	$b = 1$	0.0015	–	14.0

Note. The goodness of the fit is quantified with the root mean square error (RMSE).

The derived attenuation rates have a large spread, especially in winter. The derivation is based on the assumption that any difference in wave energy between the two buoys is caused by sea ice attenuation. This is a simplification, since the wave field would experience local variations even without the influence of sea ice, but we expect those to cancel out on average. When the wave attenuation is small compared to local variations, this sometimes leads to negative attenuation rate estimates. This is more pronounced in winter, where the buoys are closer together and the difference between wave height smaller. In fact, no significant attenuation is observed for the lowest frequency bins in winter (Figure 6). Since the distance between buoys were around 10 km, an attenuation coefficient α of 10^{-5} m^{-1} would result in a difference of power density spectrum of only 10%, which is probably too low to measure given the circumstances.

The frequency dependence of the attenuation rate is consistent with power law for both data sets (Figure 6). In spring, the fitted power coefficient

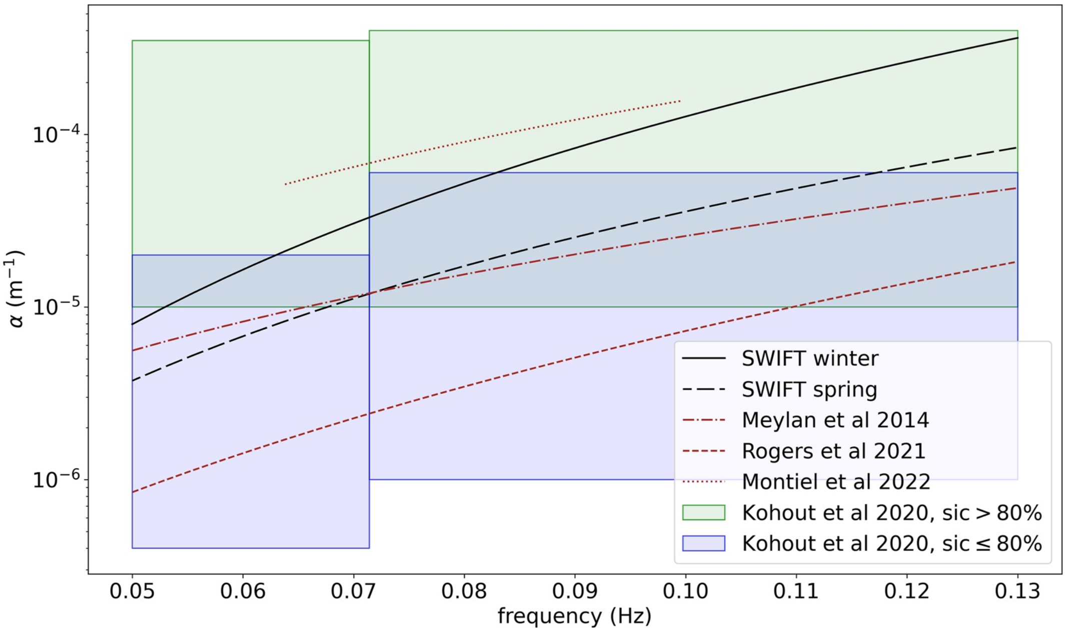

Figure 7. Comparison with other observations of spectral wave attenuation in the Antarctic MIZ: Attenuation based on the SIPEX-II data set in September 2012 Meylan et al. (2014) and various derivations from the large PIPERS data set presented by Kohout et al. (2020). Rogers et al. (2021) used the eastern subset of this data set, collected in June 2017, while the western subset, collected in April–May 2017, was used by Montiel et al. (2022).

$b = 3.3$ is consistent with the constraint $2 \leq b \leq 4$ suggested in Meylan et al. (2018). In winter, the curve fit gave $b = 4.9$, higher than the predictions by Meylan et al. (2018), but adding a constraint $2 \leq b \leq 4$ results in a very similar fit with almost the same root mean square error (RMSE) (Table 1). Since no measurable attenuation is seen for the lower frequency bins in winter, fitting a two parameter model to this data set is prone to overfitting. It is clear that b lies in the higher region of those predicted by Meylan et al. (2018), but too much weight should not be put on the exact value. For context, we also provide fits to linear and cubic relationships. The linear fit is significantly worse, with a 60% higher RMSE in spring and 30% higher RMSE in winter compared to the power law fits (Table 1). The cubic fit is very similar to the unrestricted power law fit in spring, and slightly worse in winter (Figures 6a and 6b).

The difference in attenuation between spring and winter is significant, with a roughly 5 times larger attenuation coefficient in winter than spring. A striking difference between the winter and spring deployment is the air temperature, which was well below −10°C in winter, but above −5° for the majority of the used spring data (Figure 4g). The cold air temperature during the winter deployment provide a strong heat flux out of the ocean, leading to grease ice in between and possibly below the ice floes. Interstitial grease ice has been hypothesized to affect the attenuation rate (Marquart et al., 2021). As discussed by De Carolis et al. (2021), presence of grease ice below the floes would also cause an effective ice thickness larger than the observed floe thickness, and therefore a stronger wave attenuation, which could explain the difference in attenuation between winter and spring. Thanks to extensive ice observations from the ship (de Vos et al., 2019; Skatulla et al., 2022), the ice condition is well described as first year pancake ice floes, with a granular crystal structure, surrounded by grease ice. However, due to the method used by Skatulla et al. (2022), where pancake floes were collected with a net and studied on deck, presence of grease ice below the floes would not have been detected.

In contrast to the winter deployment, the spring attenuation must be interpreted as an integrated effect over a wide range of sea ice conditions, concentration and thickness (covering all of the effects in the transition from open water to more than 100 km into the MIZ). However, this can not explain the observed difference between spring and winter, as the spring deployment is much deeper into the MIZ and in higher sea ice concentration, while experiencing a much lower attenuation rate. During the latter half of the spring deployment, the ice showed signs of melting, such as smoothed features and rounded edges of ice fragments between floes (Figure 3e). Grease ice between floes was not observed. Structural analysis of ice cores from a similar region to the SWIFT buoy deployments shows that the sea ice was composed of a more columnar crystal structure (Johnson et al., 2023). This difference in crystal structure can be reflected in the strength and elasticity of the sea ice floes (Skatulla et al., 2022), possibly impacting how they respond to the wave field. A columnar structure can have higher elasticity, which could reflect the lower attenuation rate seen in the spring deployment, despite the greater distance to the sea ice edge and higher sea ice concentration.

3.2. Change in Wave Direction

When there are simultaneous buoy measurements of wave direction in both ice and open water, the wave direction in ice is more southwards than the wave direction in open water (Figure 8a). This is seen clearly by focusing analysis from 1 November to 6 November, when we have data from both buoys and the swell wave height in open water is relatively constant (Figure 4a). Figure 8b shows the histograms of energy-weighted wave direction of the swell band ($0.05 \leq f \leq 0.13$ Hz) for the in-ice and open water data during this period. The mean direction is clearly shifted southward in ice compared to open water, while the directional spread, as defined in Equation 4 is not significantly different in and out of the ice. The directional spectra, determined from the directional moments following Thomson et al. (2018), also show a shift in wave direction with no significant change in directional spread (Figures 8d and 8e).

The southward wave direction in the sea ice is approximately perpendicular to the ice edge. We see two plausible mechanisms for this: (1) an actual change in wave direction due to refraction while traveling through sea ice, or (2) an apparent change in wave direction due to preferential wave attenuation along oblique paths. As we describe below, this data is more consistent with the first mechanism.

For the observed change in wave direction to be caused by refraction (mechanism 1), the waves would be slowing (group speed decreasing) as they propagate into the sea ice. The group speed could be evaluated by assessing the time difference between the arrival of distinct wave signals in open water and in the ice. However, the change observed herein would suggest a shift in arrival time of only a few hours, and that time difference is too small to detect in this data set that has minimal variation of wave conditions. Refraction could occur as a sharp change between open water and sea ice, resulting in a sudden change in direction as the waves reach the ice edge, or a continuous change as the waves travel through the sea ice. We know from the SWIFT onboard imagery that the sea ice changes drastically from close to the ice edge and far into the sea ice, such that a continuous change is more likely (i.e., the ice is not a homogeneous medium).

For the change in wave direction to be caused by attenuation (mechanism 2), the spread of the wave directional distribution would likely change. Surface waves in the open ocean always have significant directional spread. This means that waves reaching a certain point in the sea ice arrive from different directions, and thus travel different distances in the sea ice. The portion of the directional spectrum at oblique angles travels farther, and therefore experiences more attenuation, relative to the portion of the directional spectrum that is more perpendicular to the ice (and thus travels less distance). Thus, the oblique waves are preferentially filtered, and the perpendicular waves remain. But this mechanism would also narrow the spectrum, which is not observed. The directional spread is approximately 45° in both open water and sea ice. Although it is possible that wave scattering in the ice compensates to keep the directional spread the same during preferential attenuation, we suggest that refraction (mechanism 1) is the more likely explanation.

Although we cannot determine the reason for the change in wave direction based on this study, the finding is valuable. In situ observations of wave direction in the Antarctic MIZ rare, especially so since most wave buoys lack direction measurement. Waves perpendicular to the ice edge will reach deeper into the ice than oblique waves. Since wave penetration can accelerate loss of sea ice, ignoring ice induced direction changes in models risk leading to an underestimation of sea ice loss.

4. Summary

Two wave buoys were deployed in the Atlantic Antarctic MIZ during the SCALE cruises in austral winter and spring in 2019 to observe wave-sea ice interactions. No wave activity was observed more than 200 km into the MIZ, while the open water wave field had a significant wave height around 2–3 m in spring.

A change in wave direction between waves in open water and waves in ice was observed in the data, where the wave direction tends to be more perpendicular to the ice edge in sea ice. This could be a sign of refraction, where the propagation velocity changes with sea ice condition.

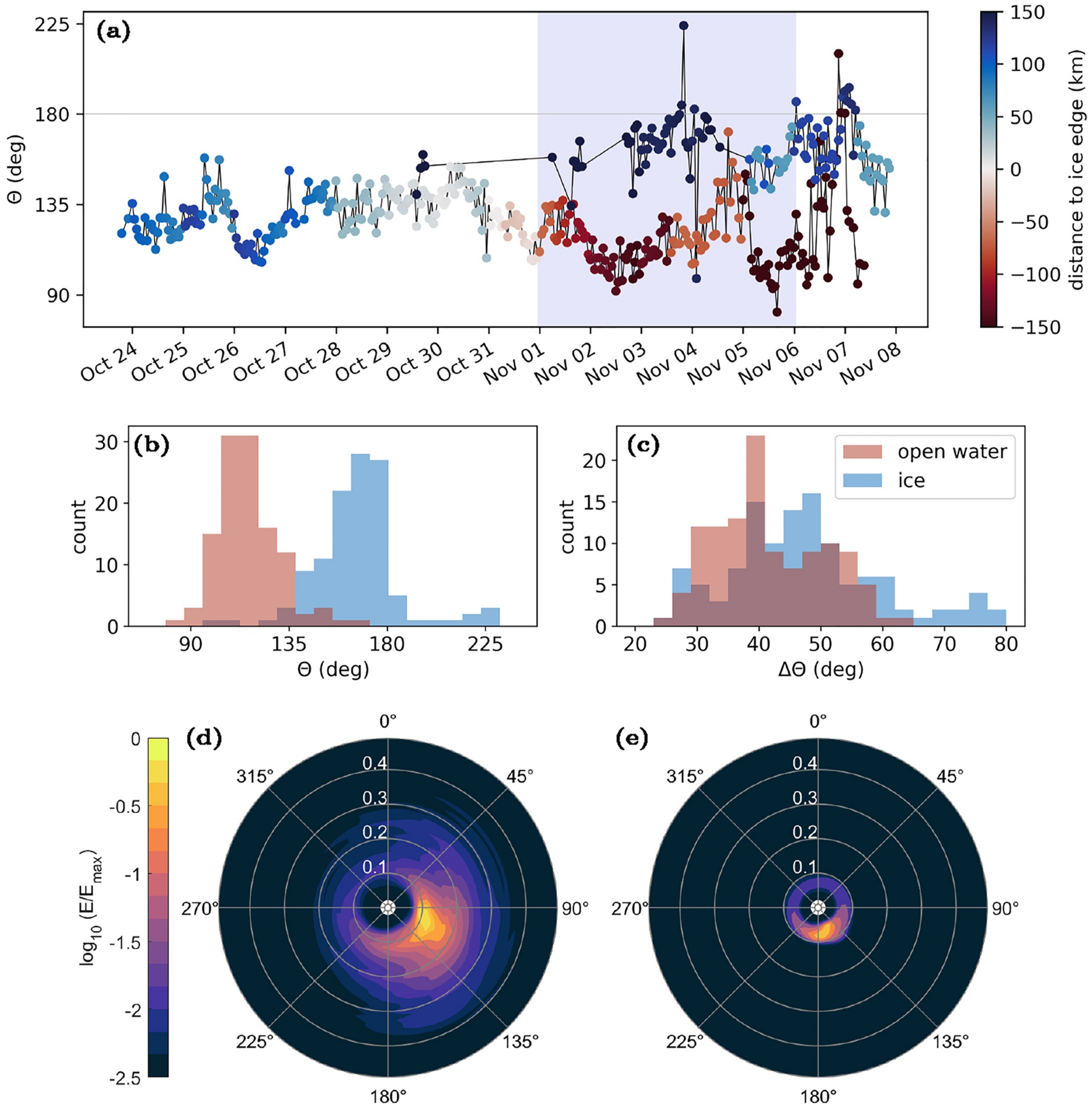

Figure 8. Springtime wave direction measured by the SWIFT buoys. (a) Time series of the energy weighted wave direction of the swell band $0.05 \leq f \leq 0.13$ (Θ), colored by meridional distance to the ice edge. Blue/positive values represent buoy in ice and red/negative values buoy in open water. The gray line marks the southward direction (180°). The shaded area marks the data used to produce panel (b–e). Histogram of (b) Θ and (c) directional spread of Θ between 1 November and 6 November for swell waves in open water (red) and in sea ice (blue). Normalized mean directional spectra over the same period for (d) open water and (e) in sea ice. The radial axis shows frequency (in Hz), covering the whole measured spectra (not only swell).

Spectral wave attenuation for wave frequencies between 0.05 and 0.13 Hz was estimated. The attenuation coefficients were close to $4 \cdot 10^{-6}$ to $7 \cdot 10^{-5}$ m^{-1} in spring, and approximately five-fold larger in winter. The frequency dependent is consistent with a power law dependency, with a power coefficient of around 4 in winter and 3.3 in spring. The difference in attenuation between spring and winter is notable, and highlights that understanding the effect of sea ice composition on wave attenuation is a critical area for improving coupled wave-sea ice models.

Data Availability Statement

The sea-ice data is made available via https://seaice.uni-bremen.de/databrowser/ (Melsheimer & Spreen, 2019). Sentinel-1 SAR imagery is available via https://dataspace.copernicus.eu/browser/ (ESA, 2019). SWIFT buoy data is published on Zenodo https://doi.org/10.5281/zenodo.7845764 (Thomson et al., 2023) and the software associated with this manuscript is published on GitHub https://github.com/stinawahlgren/roammiz-wave-seaice-interactions (Wahlgren, 2023). SWIFT buoy data has been processed using https://github.com/SASlabgroup/SWIFT-codes (Thomson, 2020).

Acknowledgments

This work was supported by the following Grants of S. Swart: Wallenberg Academy Fellowship (WAF 2015.0186), Swedish Research Council (VR 2019–04400), STINT-NRF Mobility Grant (STNT180910357293). S. Swart has received funding from the European Union's Horizon 2020 research and innovation program under Grant agreement no. 821001 (SO-CHIC). L.C Biddle's time was supported by the VR Grant 2020-04281. Alex de Klerk and Joe Talbert built and prepared the SWIFT buoys. We thank Sea Technology Services (STS), SANAP, the Captain, and crew of the S.A. Agulhas II for their field-work/technical assistance. We also thank Isabelle Giddy, Hanna Rosenthal, Johan M. Edholm, Kevin Thielen and all other participants of the SCALE cruises who helped with deployment, spotting and recovery of the SWIFT buoys. We thank two anonymous reviewers for their comments that helped improve this paper.

References

Alberello, A., Bennetts, L. G., Onorato, M., Vichi, M., MacHutchon, K., Eayrs, C., et al. (2022). Three-dimensional imaging of waves and floes in the marginal ice zone during a cyclone. *Nature Communications*, *13*(1), 4590. https://doi.org/10.1038/s41467-022-32036-2

Ardhuin, F., Otero, M., Merrifield, S., Grouazel, A., & Terrill, E. (2020). Ice breakup controls dissipation of wind waves across southern ocean sea ice. *Geophysical Research Letters*, *47*(13), e2020GL087699. https://doi.org/10.1029/2020GL087699

Brouwer, J., Fraser, A. D., Murphy, D. J., Wongpan, P., Alberello, A., Kohout, A., et al. (2022). Altimetric observation of wave attenuation through the Antarctic marginal ice zone using ICESat-2. *The Cryosphere*, *16*(6), 2325–2353. https://doi.org/10.5194/tc-16-2325-2022

Cooper, V. T., Roach, L. A., Thomson, J., Brenner, S. D., Smith, M. M., Meylan, M. H., & Bitz, C. M. (2022). Wind waves in sea ice of the western Arctic and a global coupled wave-ice model. *Philosophical Transactions of the Royal Society A: Mathematical, Physical & Engineering Sciences*, *380*(2235), 20210258. https://doi.org/10.1098/rsta.2021.0258

De Carolis, G., Olla, P., & De Santi, F. (2021). SAR image wave spectra to retrieve the thickness of grease-pancake sea ice using viscous wave propagation models. *Scientific Reports*, *11*(1), 2733. https://doi.org/10.1038/s41598-021-82228-x

de Vos, M., Ramjukadh, C.-L., Liesker, C. G., de Villiers, M., & Lyttle, C. T. (2019). *Southern ocean marginal ice zone photographs from a 2019 winter research cruise (SA Agulhas II)*. PANGAEA. https://doi.org/10.1594/PANGAEA.905497

ESA. (2019). Copernicus Sentinel data (2019) [Dataset]. Retrieved from https://dataspace.copernicus.eu

Hošeková, L., Malila, M. P., Rogers, W. E., Roach, L. A., Eidam, E., Rainville, L., et al. (2020). Attenuation of ocean surface waves in pancake and frazil sea ice along the coast of the Chukchi Sea. *Journal of Geophysical Research: Oceans*, *125*(12), e2020JC016746. https://doi.org/10.1029/2020JC016746

Johnson, S., Audh, R. R., De Jager, W., Matlakala, B., Vichi, M., Womack, A., & Rampai, T. (2023). Physical and morphological properties of first-year Antarctic sea ice in the spring marginal ice zone of the Atlantic-Indian sector. *Journal of Glaciology*, *1–14*, 1–14. https://doi.org/10.1017/jog.2023.21

Kohout, A. L., Smith, M., Roach, L. A., Williams, G., Montiel, F., & Williams, M. J. M. (2020). Observations of exponential wave attenuation in Antarctic sea ice during the PIPERS campaign. *Annals of Glaciology*, *61*(82), 196–209. https://doi.org/10.1017/aog.2020.36

Kousal, J., Voermans, J. J., Liu, Q., Heil, P., & Babanin, A. V. (2022). A two-part model for wave-sea ice interaction: Attenuation and break-up. *Journal of Geophysical Research: Oceans*, *127*(5), e2022JC018571. https://doi.org/10.1029/2022JC018571

Langhorne, P. J., Squire, V. A., Fox, C., & Haskell, T. G. (1998). Break-up of sea ice by ocean waves. *Annals of Glaciology*, *27*, 438–442. https://doi.org/10.3189/S0260305500017869

Marquart, R., Bogaers, A., Skatulla, S., Alberello, A., Toffoli, A., Schwarz, C., & Vichi, M. (2021). A computational fluid dynamics model for the small-scale dynamics of wave, ice floe and interstitial grease ice interaction. *Fluids*, *6*(5), 176. https://doi.org/10.3390/fluids6050176

Massom, R. A., Scambos, T. A., Bennetts, L. G., Reid, P., Squire, V. A., & Stammerjohn, S. E. (2018). Antarctic ice shelf disintegration triggered by sea ice loss and ocean swell. *Nature*, *558*(7710), 383–389. https://doi.org/10.1038/s41586-018-0212-1

Melsheimer, C. (2019). ASI version 5 sea ice concentration user guide.

Melsheimer, C., & Spreen, G. (2019). AMSR2 ASI sea ice concentration data, Antarctic, version 5.4 (NetCDF) (July 2012–December 2019) [Dataset]. PANGAEA. https://doi.org/10.1594/PANGAEA.898400

Meylan, M. H., Bennetts, L. G., & Kohout, A. L. (2014). In situ measurements and analysis of ocean waves in the Antarctic marginal ice zone. *Geophysical Research Letters*, *41*(14), 5046–5051. https://doi.org/10.1002/2014GL060809

Meylan, M. H., Bennetts, L. G., Mosig, J. E. M., Rogers, W. E., Doble, M. J., & Peter, M. A. (2018). Dispersion relations, power laws, and energy loss for waves in the marginal ice zone. *Journal of Geophysical Research: Oceans*, *123*(5), 3322–3335. https://doi.org/10.1002/2018JC013776

Montiel, F., Kohout, A. L., & Roach, L. A. (2022). Physical drivers of ocean wave attenuation in the marginal ice zone. *Journal of Physical Oceanography*, *52*(5), 889–906. https://doi.org/10.1175/JPO-D-21-0240.1

Nose, T., Waseda, T., Kodaira, T., & Inoue, J. (2020). Satellite-retrieved sea ice concentration uncertainty and its effect on modelling wave evolution in marginal ice zones. *The Cryosphere*, *14*(6), 2029–2052. https://doi.org/10.5194/tc-14-2029-2020

Rogers, W., Meylan, M. H., & Kohout, A. L. (2021). Estimates of spectral wave attenuation in Antarctic sea ice, using model/data inversion. *Cold Regions Science and Technology*, *182*, 103198. https://doi.org/10.1016/j.coldregions.2020.103198

Rogers, W., Posey, P., Li, L., & Allard, R. (2018). Forecasting and hindcasting waves in and near the marginal ice zone: Wave modeling and the ONR sea state field experiment. Retrieved from https://www.semanticscholar.org/paper/Forecasting-and-Hindcasting-Waves-In-and-Near-the-Rogers-Posey/5583f6d20c399b17bbebd4efc347c0bb0b69a01a

Ryan-Keogh, T., & Vichi, M. (2022). SCALE-WIN19 & SCALE-SPR19 cruise report. (Technical Report). Zenodo. https://doi.org/10.5281/zenodo.5906324

Shen, H. H., & Ackley, S. F. (1991). A one-dimensional model for wave-induced ice-floe collisions. *Annals of Glaciology*, *15*, 87–95. https://doi.org/10.3189/1991AoG15-1-87-95

Skatulla, S., Audh, R. R., Cook, A., Hepworth, E., Johnson, S., Lupascu, D. C., et al. (2022). Physical and mechanical properties of winter first-year ice in the Antarctic marginal ice zone along the Good Hope Line. *The Cryosphere*, *16*(7), 2899–2925. https://doi.org/10.5194/tc-16-2899-2022

Squire, V. A. (2022). A prognosticative synopsis of contemporary marginal ice zone research. *Philosophical Transactions of the Royal Society A: Mathematical, Physical & Engineering Sciences*, *380*(2235), 20220094. https://doi.org/10.1098/rsta.2022.0094

Swart, S., du Plessis, M. D., Thompson, A. F., Biddle, L. C., Giddy, I., Linders, T., et al. (2020). Submesoscale fronts in the Antarctic marginal ice zone and their response to wind forcing. *Geophysical Research Letters*, *47*(6), e2019GL086649. https://doi.org/10.1029/2019GL086649

Thomson, J. (2012). Wave breaking dissipation observed with "SWIFT" drifters. *Journal of Atmospheric and Oceanic Technology*, *29*(12), 1866–1882. https://doi.org/10.1175/JTECH-D-12-00018.1

Thomson, J. (2020). SWIFT codes: 1 Jan 2020 [Software]. Retrieved from https://github.com/SASlabgroup/SWIFT-codes

Thomson, J., Biddle, L. C., Wahlgren, S., & Swart, S. (2023). Direct observations of wave-sea ice interactions in the Antarctic marginal ice zone [Dataset]. Zenodo. https://doi.org/10.5281/zenodo.7845764

Thomson, J., Girton, J. B., Jha, R., & Trapani, A. (2018). Measurements of directional wave spectra and wind stress from a wave glider autonomous surface vehicle. *Journal of Atmospheric and Oceanic Technology*, *35*(2), 347–363. https://doi.org/10.1175/JTECH-D-17-0091.1

Thomson, J., Hošeková, L., Meylan, M. H., Kohout, A. L., & Kumar, N. (2021). Spurious rollover of wave attenuation rates in sea ice caused by noise in field measurements. *Journal of Geophysical Research: Oceans*, *126*(3), e2020JC016606. https://doi.org/10.1029/2020JC016606

Thomson, J., Talbert, J., de Klerk, A., Brown, A., Schwendeman, M., Goldsmith, J., et al. (2015). Biofouling effects on the response of a wave measurement buoy in deep water. *Journal of Atmospheric and Oceanic Technology*, *32*(6), 1281–1286. https://doi.org/10.1175/JTECH-D-15-0029.1

Toffoli, A., Bennetts, L. G., Meylan, M. H., Cavaliere, C., Alberello, A., Elsnab, J., & Monty, J. P. (2015). Sea ice floes dissipate the energy of steep ocean waves. *Geophysical Research Letters*, *42*(20), 8547–8554. https://doi.org/10.1002/2015GL065937

Vichi, M. (2022). An indicator of sea ice variability for the Antarctic marginal ice zone. *The Cryosphere*, *16*(10), 4087–4106. https://doi.org/10.5194/tc-16-4087-2022

Vichi, M., Eayrs, C., Alberello, A., Bekker, A., Bennetts, L., Holland, D., et al. (2019). Effects of an explosive polar cyclone crossing the Antarctic marginal ice zone. *Geophysical Research Letters*, *46*(11), 5948–5958. https://doi.org/10.1029/2019GL082457

Voermans, J. J., Babanin, A. V., Thomson, J., Smith, M. M., & Shen, H. H. (2019). Wave attenuation by sea ice turbulence. *Geophysical Research Letters*, *46*(12), 6796–6803. https://doi.org/10.1029/2019GL082945

Wadhams, P., Squire, V. A., Goodman, D. J., Cowan, A. M., & Moore, S. C. (1988). The attenuation rates of ocean waves in the marginal ice zone. *Journal of Geophysical Research*, *93*(C6), 6799–6818. https://doi.org/10.1029/JC093iC06p06799

Wahlgren, S. (2023). Roammiz-wave-sea ice-interactions [Software]. Retrieved from https://github.com/stinawahlgren/roammiz-wave-seaice-interactions

Womack, A., Vichi, M., Alberello, A., & Toffoli, A. (2022). Atmospheric drivers of a winter-to-spring Lagrangian sea-ice drift in the Eastern Antarctic marginal ice zone. *Journal of Glaciology*, *68*(271), 999–1013. https://doi.org/10.1017/jog.2022.14

Worby, A., & Allison, I. (1999). A technique for making ship-based observations of Antarctic sea ice thickness and characteristics. Part I. Observational techniques and results. *Antarctic CRC Research Report*, *14*.

Young, I. R., Fontaine, E., Liu, Q., & Babanin, A. V. (2020). The wave climate of the southern ocean. *Journal of Physical Oceanography*, *50*(5), 1417–1433. https://doi.org/10.1175/JPO-D-20-0031.1